



## Heatline analysis of heat recovery and thermal transport in materials confined within triangular cavities

Tanmay Basak<sup>a</sup>, G. Aravind<sup>a</sup>, S. Roy<sup>b</sup>, A.R. Balakrishnan<sup>a,\*</sup>

<sup>a</sup> Department of Chemical Engineering, Indian Institute of Technology Madras, Chennai 600 036, India

<sup>b</sup> Department of Mathematics, Indian Institute of Technology Madras, Chennai 600 036, India

### ARTICLE INFO

#### Article history:

Received 15 April 2009

Received in revised form 13 January 2010

Accepted 17 January 2010

Available online 11 May 2010

#### Keywords:

Material processing

Heatlines

Triangular cavity

Natural convection

### ABSTRACT

Heat recovery from hot fluids in material processing industries is important for environmental and thermal management. Present work involves numerical visualization of heat flow in entrapped cavities filled with hot materials. The concept of heatline is used to visualize the heat energy trajectory. The system involves entrapped triangular cavities filled with hot fluid ( $Pr = 0.015, 0.026, 0.7$  and  $1000$ ). At low Rayleigh number ( $Ra$ ), it is found that the heatlines are smooth and perfectly normal to the isotherms indicating the dominance of conduction for both the triangles. As  $Ra$  increases, flow slowly becomes convection dominant. Multiple heat flow circulations with high intensity are formed within the lower triangular domain especially for low  $Pr$  numbers, whereas, less intense convective heat flow circulations are observed for the upper triangle. Multiple circulations are absent for both the triangular domains involving fluids with higher  $Pr$  numbers. It is observed that the heat transfer rates are monotonic for the upper triangle whereas a few local maxima in heat transfer rates occur for smaller  $Pr$  within lower triangular domain. Overall, fluid with any  $Pr$  may be useful for enhanced heat transfer within the upper triangle but fluid with high  $Pr$  may be preferred for the lower triangle.

© 2010 Elsevier Ltd. All rights reserved.

### 1. Introduction

Researchers have been interested in the study of indirect heating or cooling processes because of its many industrial and day-to-day applications [1–4]. Indirect heat transfer of fluids have applications in material processing industries, geophysical processes, pollution control, etc. [5–14]. A few applications involving food processing industries and molten metal processing require comprehensive knowledge of the heat transfer processes involved [15,16]. Such applications may be analyzed in two ways: experimental and numerical. Since experimental analysis is associated with high cost, numerical method of analyzing is generally preferred.

Over the recent past, the importance of heat exchangers has increased because of energy conservation, conversion, recovery, and implementation of new energy sources. Various material processing and environmental treatments such as combustion, thermal pollution, air pollution, water pollution and waste disposal signify the importance of heat exchangers [17–22]. Heat exchangers are also used extensively in air conditioning and refrigeration, cryo-

genic, heat recovery, alternate fuels and manufacturing industries, etc.

Large amount of heat may be generated for systems involving combustion, hot material processing, food processing, etc. Excessive heat may be detrimental to the systems or hot materials (e.g. food processing) and a part of the heat may be recovered by other contacting fluids. The present study analyzes the heat recovery from hot fluids passing parallel to the hot plates and heat may be transported to the entrapped fluid between a stack of tubes. The cold fluid is pumped through the square tubes such that inclined walls of the entrapped triangular cavity are maintained at a constant cold temperature. A case study may be visualized as an assembly of square tubes adjacent to each other and a pair of triangular cavities is filled with fluid (Fig. 1a). The proposed system for the present study is a coupled triangular cavity system with cold inclined walls and hot horizontal walls. The computational domain with respective boundary conditions is shown in Fig. 1b. The aspect ratio is maintained at 2:1 for both the triangles. The heat transfer analysis with flow circulations within such triangular cavities requires an in-depth knowledge of fluid flow and temperature distribution in triangular cavities.

Researchers have shown significant amount of interest in the field of indirect heat recovery through cavities or channels [23–27]. However, for heat transfer within triangular cavities, there have been only a few studies carried out earlier. Salmun

\* Corresponding author. Tel.: +91 44 2257 4154; fax: +91 44 2257 0509.

E-mail addresses: [tanmay@iitm.ac.in](mailto:tanmay@iitm.ac.in) (T. Basak), [sjroy@iitm.ac.in](mailto:sjroy@iitm.ac.in) (S. Roy), [arbala@iitm.ac.in](mailto:arbala@iitm.ac.in) (A.R. Balakrishnan).

## Nomenclature

$g$	acceleration due to gravity ( $\text{m s}^{-2}$ )
$k$	thermal conductivity ( $\text{W m}^{-1} \text{K}^{-1}$ )
$L$	height of the triangular cavity (m)
$N$	total number of nodes
$Nu$	Nusselt number
$p$	pressure (Pa)
$P$	dimensionless pressure
$Pr$	Prandtl number
$R$	residual of weak form
$Ra$	Rayleigh number
$T$	temperature (K)
$T_h$	temperature of hot inclined wall (K)
$T_c$	temperature of cold top wall (K)
$u$	$x$ component of velocity
$U$	$x$ component of dimensionless velocity
$v$	$y$ component of velocity
$V$	$y$ component of dimensionless velocity
$X$	dimensionless distance along $x$ -coordinate
$x$	distance along $x$ -coordinate
$Y$	dimensionless distance along $y$ -coordinate
$y$	distance along $y$ -coordinate

## Greek symbols

$\alpha$	thermal diffusivity ( $\text{m}^2 \text{s}^{-1}$ )
$\beta$	volume expansion coefficient ( $\text{K}^{-1}$ )
$\gamma$	penalty parameter
$\Gamma$	boundary
$\theta$	dimensionless temperature
$\nu$	kinematic viscosity ( $\text{m}^2 \text{s}^{-1}$ )
$\rho$	density ( $\text{kg m}^{-3}$ )
$\Phi$	basis functions
$\psi$	streamfunction
$\Pi$	heatfunction

## Subscripts

$i$	residual number
$k$	node number
$l$	left wall
$r$	right wall
$h$	horizontal wall

[28] analyzed the convection patterns in a triangular domain. Karyakin et al. [29] studied the transient natural convection in triangular enclosures. The analysis of laminar natural convection in a triangular enclosure was carried out by Del Campo et al. [30]. Wu et al. [31] carried out a numerical study of natural convection in crystallization processes. However, many of the recent works are targeted more towards the application aspect of the process. Ridouane et al. [32] and Ridouane and Campo [33] studied extensively the natural convection in an isosceles triangle and right triangular cavity in their work. Ben-Nakhi and Mahmoud [34] studied the natural convection in roof cavities inside buildings. Varol et al. [35,36] carried out extensive studies on natural convection in triangular enclosures in their work. Other recent investigations on natural convection in triangular enclosure have been reported by various researchers [37–41].

Even though there has been a considerable amount of work on heat transfer within triangular cavities reported in the literature, the present work focuses on the distribution of heat flow associated with natural convection within entrapped triangular cavities. The heat flow distributions are analyzed with the heatlines method. The concept of heatlines was first introduced by Kimura and Bejan [42] and Bejan [43]. Heatlines represent the heat energy flow trajectory in the system. The mathematical formulation of heatline method uses the heatfunction. Various studies have been reported on heatfunction by Bello-Ochende [44], Costa [45–48], Mukhopadhyay et al. [49], Dalal and Das [50] and Deng and Tang [51]. Although a number of studies on heatlines have been carried out earlier [42–51], the analysis of heat flow via heatlines within triangular cavities is yet to be reported in the literature.

The aim of the current work is as follows: to analyze the heat transfer in two entrapped triangular domains (Fig. 1b), to visualize the heat flow in the domains and finally to recommend efficient heat transfer to the entrapped cold fluid. The governing equations for heat and fluid flow are solved using the Galerkin finite element method with penalty parameter. The Poisson equations for streamfunction and heatfunction are also solved using the Galerkin method. The jump discontinuity in Dirichlet type of wall boundary conditions for temperature at corner points corresponds to computational singularities. The problem is tackled by considering the

average temperature of the two walls at the corner and keeping the adjacent grid nodes at the respective wall temperatures in a similar to earlier work [52,53]. The key parameters for the analysis are considered as the Prandtl number, Rayleigh number and Nusselt number. Wide range of Prandtl numbers are assumed from 0.015 to 1000 and this wide range of Prandtl number ensures that almost all types of fluids of industrial importance is covered in the present study. Small Prandtl numbers ( $Pr = 0.015$ ) correspond to that of molten metals,  $Pr = 0.7$  is for air and similar fluids,  $Pr = 10$  is usually for salt water and high  $Pr$  values ( $Pr = 1000$ ) are associated with olive oil and machine oils. Finally, heat recovery for various fluids has been assessed via computing heat transfer rates or Nusselt numbers.

## 2. Governing equations and solution procedure

### 2.1. Temperature and velocity

The fluid properties are assumed to be constant except the density variation which is determined according to the Boussinesq approximation. This approximation is used in the field of buoyancy driven flows and it is based on the fact that variation of density with the temperature can be neglected, except in the body force term. The dimension in  $Z$ -direction has been assumed to be sufficiently large such that two-dimensional approximation of temperature and flow fields are adequate. Under these assumptions, the governing equations for steady two dimensional, laminar, incompressible flows can be written in dimensionless form as:

$$\frac{\partial U}{\partial X} + \frac{\partial V}{\partial Y} = 0, \quad (1)$$

$$U \frac{\partial U}{\partial X} + V \frac{\partial U}{\partial Y} = -\frac{\partial P}{\partial X} + Pr \left( \frac{\partial^2 U}{\partial X^2} + \frac{\partial^2 U}{\partial Y^2} \right), \quad (2)$$

$$U \frac{\partial V}{\partial X} + V \frac{\partial V}{\partial Y} = -\frac{\partial P}{\partial Y} + Pr \left( \frac{\partial^2 V}{\partial X^2} + \frac{\partial^2 V}{\partial Y^2} \right) + RaPr\theta, \quad (3)$$

$$U \frac{\partial \theta}{\partial X} + V \frac{\partial \theta}{\partial Y} = \frac{\partial^2 \theta}{\partial X^2} + \frac{\partial^2 \theta}{\partial Y^2}, \quad (4)$$

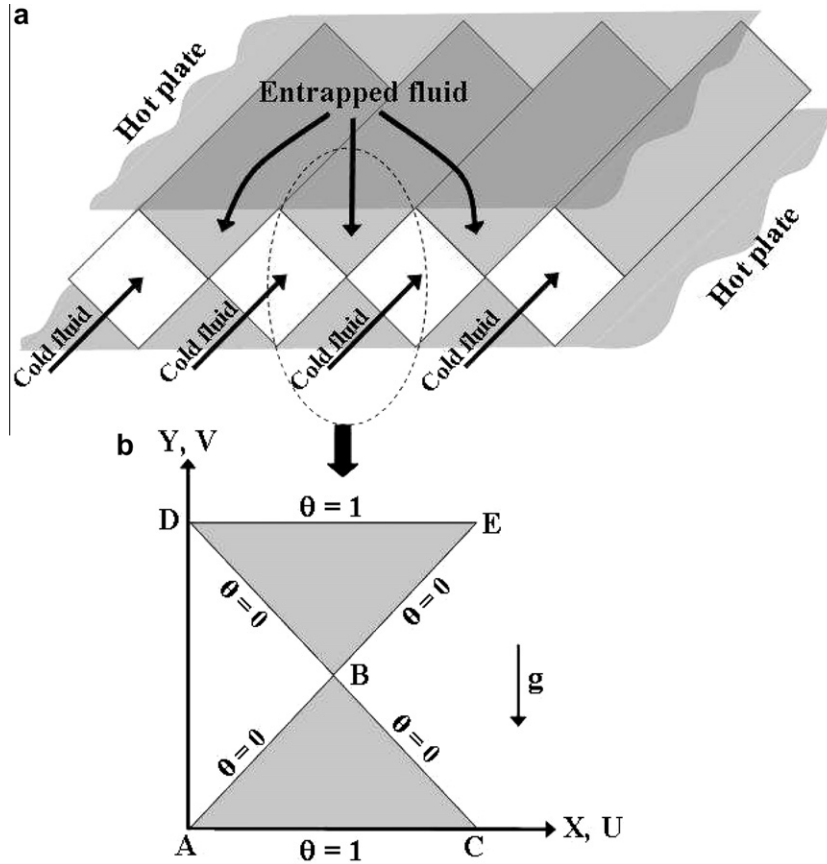


Fig. 1. (a) Schematic diagram of the physical system and (b) computational domain with the boundary conditions.

where

$$X = \frac{x}{L}, \quad Y = \frac{y}{L}, \quad U = \frac{uL}{\alpha}, \quad V = \frac{vL}{\alpha}, \quad \theta = \frac{T - T_c}{T_h - T_c}, \quad (5)$$

$$P = \frac{pL^2}{\rho\alpha^2}, \quad Pr = \frac{\nu}{\alpha}, \quad Ra = \frac{g\beta(T_h - T_c)L^3Pr}{\nu^2}.$$

Here,  $X$  and  $Y$  are the dimensionless distances along  $x$ - and  $y$ -coordinates, respectively,  $U$  and  $V$  are the corresponding velocity components along the coordinates,  $\theta$  denotes the dimensionless temperature and  $P$  denotes the dimensionless pressure. The dimensionless parameters  $Pr$  and  $Ra$  denote Prandtl number and Rayleigh number, respectively.

The cold fluid is pumped through the square tubes. The flow rate may be sufficiently high such that cold fluid may act as a sink and the inclined wall is maintained at a constant cold temperature, i.e. Dirichlet boundary conditions. The horizontal top and bottom walls are maintained hot (constant Dirichlet temperature) as shown in Fig. 1a. The constant temperature at the hot wall is due to the flow of hot gases over the top wall and below the bottom wall. Based on the physical situation, the boundary conditions for velocity components and temperature within the entrapped lower triangular cavity are as follows (Fig. 1b):

$$U(X, 0) = V(X, 0) = 0 \quad \text{on AC},$$

$$U(X, Y) = V(X, Y) = 0 \quad \text{on AB},$$

$$U(X, Y) = V(X, Y) = 0 \quad \text{on BC},$$

(6)

and

$$\theta(X, 0) = 1 \quad \text{on AC},$$

$$\theta(X, Y) = 0 \quad \text{on AB},$$

$$\theta(X, Y) = 0 \quad \text{on BC}. \quad (7)$$

The boundary conditions for velocity components and temperature within the upper triangle is as follows (Fig. 1b):

$$U(X, 2) = V(X, 2) = 0 \quad \text{on DE},$$

$$U(X, Y) = V(X, Y) = 0 \quad \text{on BE},$$

$$U(X, Y) = V(X, Y) = 0 \quad \text{on BD},$$

(8)

and

$$\theta(X, 2) = 1 \quad \text{on DE},$$

$$\theta(X, Y) = 0 \quad \text{on BE},$$

$$\theta(X, Y) = 0 \quad \text{on BD}. \quad (9)$$

The continuity equation (Eq. (1)) is used as a constraint due to mass conservation and this constraint can be used to obtain the pressure distribution. The momentum and energy balance equations (Eqs. (2)–(4)) are solved using Galerkin finite element method. In order to solve Eqs. (2) and (3), penalty finite element method has been employed to eliminate the pressure  $P$  with a penalty parameter  $\gamma$  and the incompressibility criteria, given by Eq. (1) via following relationship [54]:

$$P = -\gamma \left( \frac{\partial U}{\partial X} + \frac{\partial V}{\partial Y} \right). \quad (10)$$

For large values of  $\gamma$ , the above equation satisfies the continuity equation (Eq. (1)). Typically  $\gamma = 10^7$  yields consistent solutions. Applying Eq. (10), the momentum balance equations (Eqs. (2) and (3)) are reduced to

$$U \frac{\partial U}{\partial X} + V \frac{\partial U}{\partial Y} = \gamma \frac{\partial}{\partial X} \left( \frac{\partial U}{\partial X} + \frac{\partial V}{\partial Y} \right) + Pr \left( \frac{\partial^2 U}{\partial X^2} + \frac{\partial^2 U}{\partial Y^2} \right) \quad (11)$$

and

$$U \frac{\partial V}{\partial X} + V \frac{\partial V}{\partial Y} = \gamma \frac{\partial}{\partial Y} \left( \frac{\partial U}{\partial X} + \frac{\partial V}{\partial Y} \right) + Pr \left( \frac{\partial^2 V}{\partial X^2} + \frac{\partial^2 V}{\partial Y^2} \right) + Ra Pr \theta. \quad (12)$$

Expanding velocity components ( $U, V$ ) and temperature ( $\theta$ ) using basis set  $\{\Phi_k\}_{k=1}^N$  as,

$$U \approx \sum_{k=1}^N U_k \Phi_k(X, Y), \quad V \approx \sum_{k=1}^N V_k \Phi_k(X, Y), \quad \text{and} \quad \theta \approx \sum_{k=1}^N \theta_k \Phi_k(X, Y), \quad (13)$$

Galerkin finite element method yields the following non-linear residual equation for Eqs. (11), (12) and (4), respectively, at nodes of internal domain  $\Omega[\triangle ABC$  or  $\triangle BDE]$ .

$$R_i^{(1)} = \sum_{k=1}^N U_k \int_{\Omega} \left[ \left( \sum_{k=1}^N U_k \Phi_k \right) \frac{\partial \Phi_k}{\partial X} + \left( \sum_{k=1}^N V_k \Phi_k \right) \frac{\partial \Phi_k}{\partial Y} \right] \Phi_i dX dY + \gamma \left[ \sum_{k=1}^N U_k \int_{\Omega} \frac{\partial \Phi_i}{\partial X} \frac{\partial \Phi_k}{\partial X} dX dY + \sum_{k=1}^N V_k \int_{\Omega} \frac{\partial \Phi_i}{\partial X} \frac{\partial \Phi_k}{\partial Y} dX dY \right] + Pr \sum_{k=1}^N U_k \int_{\Omega} \left[ \frac{\partial \Phi_i}{\partial X} \frac{\partial \Phi_k}{\partial X} + \frac{\partial \Phi_i}{\partial Y} \frac{\partial \Phi_k}{\partial Y} \right] dX dY, \quad (14)$$

$$R_i^{(2)} = \sum_{k=1}^N V_k \int_{\Omega} \left[ \left( \sum_{k=1}^N U_k \Phi_k \right) \frac{\partial \Phi_k}{\partial X} + \left( \sum_{k=1}^N V_k \Phi_k \right) \frac{\partial \Phi_k}{\partial Y} \right] \Phi_i dX dY + \gamma \left[ \sum_{k=1}^N U_k \int_{\Omega} \frac{\partial \Phi_i}{\partial Y} \frac{\partial \Phi_k}{\partial X} dX dY + \sum_{k=1}^N V_k \int_{\Omega} \frac{\partial \Phi_i}{\partial Y} \frac{\partial \Phi_k}{\partial Y} dX dY \right] + Pr \sum_{k=1}^N V_k \int_{\Omega} \left[ \frac{\partial \Phi_i}{\partial X} \frac{\partial \Phi_k}{\partial X} + \frac{\partial \Phi_i}{\partial Y} \frac{\partial \Phi_k}{\partial Y} \right] dX dY - Ra Pr \int_{\Omega} \left( \sum_{k=1}^N \theta_k \Phi_k \right) \Phi_i dX dY, \quad (15)$$

and

$$R_i^{(3)} = \sum_{k=1}^N \theta_k \int_{\Omega} \left[ \left( \sum_{k=1}^N U_k \Phi_k \right) \frac{\partial \Phi_k}{\partial X} + \left( \sum_{k=1}^N V_k \Phi_k \right) \frac{\partial \Phi_k}{\partial Y} \right] \Phi_i dX dY + \sum_{k=1}^N \theta_k \int_{\Omega} \left[ \frac{\partial \Phi_i}{\partial X} \frac{\partial \Phi_k}{\partial X} + \frac{\partial \Phi_i}{\partial Y} \frac{\partial \Phi_k}{\partial Y} \right] dX dY. \quad (16)$$

Bi-quadratic basis functions with three point Gaussian quadrature is used to evaluate the integrals in residual equations except the second term in Eqs. (14) and (15). The second term containing the penalty parameter ( $\gamma$ ) is evaluated with two point Gaussian quadrature (reduced integration penalty formulation [54]). The non-linear residual equations (Eqs. (14)–(16)) are solved using Newton–Raphson method to determine the coefficients of the expansions in Eq. (13).

### 2.2. Streamfunction and heatfunction

The fluid motion is displayed using the streamfunction ( $\psi$ ) obtained from velocity components  $U$  and  $V$  for both the triangles. The relationships between streamfunction,  $\psi$  and velocity components for two-dimensional flows are

$$U = \frac{\partial \psi}{\partial Y} \quad \text{and} \quad V = -\frac{\partial \psi}{\partial X}, \quad (17)$$

which yield a single equation

$$\frac{\partial^2 \psi}{\partial X^2} + \frac{\partial^2 \psi}{\partial Y^2} = \frac{\partial U}{\partial Y} - \frac{\partial V}{\partial X}. \quad (18)$$

The sign convention is as follows: positive sign of  $\psi$  denotes anti-clockwise circulation and clockwise circulation is represented by negative sign of  $\psi$ . The no-slip condition is valid at all boundaries as there is no cross flow, hence  $\psi = 0$  is used for boundaries.

Expanding the streamfunction ( $\psi$ ) using the basis set  $\{\Phi_k\}^N$  as  $\psi = \sum_{k=1}^N \psi_k \Phi_k(X, Y)$  and the relationship for  $U$  and  $V$  from Eq. (13), Galerkin finite element method yields the following linear residual equation for Eq. (18):

$$R_i^s = \sum_{k=1}^N \psi_k \int_{\Omega} \left[ \frac{\partial \Phi_i}{\partial X} \frac{\partial \Phi_k}{\partial X} + \frac{\partial \Phi_i}{\partial Y} \frac{\partial \Phi_k}{\partial Y} \right] dX dY - \int_{\Gamma} \Phi_i \mathbf{n} \cdot p \nabla \psi d\Gamma + \sum_{k=1}^N U_k \int_{\Omega} \Phi_i \frac{\partial \Phi_k}{\partial Y} dX dY - \sum_{k=1}^N V_k \int_{\Omega} \Phi_i \frac{\partial \Phi_k}{\partial X} dX dY. \quad (19)$$

The heat flow within the enclosure is displayed using the heatfunction ( $\Pi$ ) obtained from conductive heat fluxes ( $-\frac{\partial \theta}{\partial X}, -\frac{\partial \theta}{\partial Y}$ ) as well as convective heat fluxes ( $U\theta, V\theta$ ). The heatfunction satisfies the steady energy balance equation (Eq. (4)) such that

$$\frac{\partial \Pi}{\partial Y} = U\theta - \frac{\partial \theta}{\partial X}, \quad (20)$$

$$-\frac{\partial \Pi}{\partial X} = V\theta - \frac{\partial \theta}{\partial Y},$$

which yield a single equation

$$\frac{\partial^2 \Pi}{\partial X^2} + \frac{\partial^2 \Pi}{\partial Y^2} = \frac{\partial}{\partial Y} (U\theta) - \frac{\partial}{\partial X} (V\theta). \quad (21)$$

The basis of sign convention for heatfunction is based on the concept that heat flows from hot to cold surface and positive heatfunction corresponds to anti-clockwise heat flow. Expanding the heatfunction ( $\Pi$ ) using the basis set  $\{\Phi_k\}^N$  as  $\Pi = \sum_{k=1}^N \Pi_k \Phi_k(X, Y)$  and the relationship for  $U, V$  and  $\theta$  from Eq. (13), the Galerkin finite element method yields the following linear residual equation for Eq. (21):

$$R_i^h = \sum_{k=1}^N \Pi_k \int_{\Omega} \left[ \frac{\partial \Phi_i}{\partial X} \frac{\partial \Phi_k}{\partial X} + \frac{\partial \Phi_i}{\partial Y} \frac{\partial \Phi_k}{\partial Y} \right] dX dY - \int_{\Gamma} \Phi_i \mathbf{n} \cdot p \nabla \Pi d\Gamma + \sum_{k=1}^N U_k \int_{\Omega} \left( \sum_{k=1}^N \theta_k \Phi_k \right) \Phi_i \frac{\partial \Phi_k}{\partial Y} dX dY + \sum_{k=1}^N \theta_k \int_{\Omega} \left( \sum_{k=1}^N U_k \Phi_k \right) \Phi_i \frac{\partial \Phi_k}{\partial Y} dX dY - \sum_{k=1}^N V_k \int_{\Omega} \left( \sum_{k=1}^N \theta_k \Phi_k \right) \Phi_i \frac{\partial \Phi_k}{\partial X} dX dY - \sum_{k=1}^N \theta_k \int_{\Omega} \left( \sum_{k=1}^N V_k \Phi_k \right) \Phi_i \frac{\partial \Phi_k}{\partial X} dX dY. \quad (22)$$

The residual equation (Eq. (22)) is further supplemented with various Dirichlet and Neumann boundary conditions in order to obtain a unique solution of Eq. (21). Neumann boundary conditions for  $\Pi$  are obtained due to isothermal (hot or cold) wall as derived from Eq. (20). It may be noted that, the normal derivatives ( $\mathbf{n} \cdot p \nabla \Pi$ ) are zero ( $\mathbf{n} \cdot p \nabla \Pi = 0$ ) for all the isothermal walls of  $\triangle ABC$  and  $\triangle BDE$ .

In order to obtain the unique non-homogeneous solution of  $\Pi$ , the following non-homogeneous Dirichlet boundary conditions have been derived based on Eq. (20).

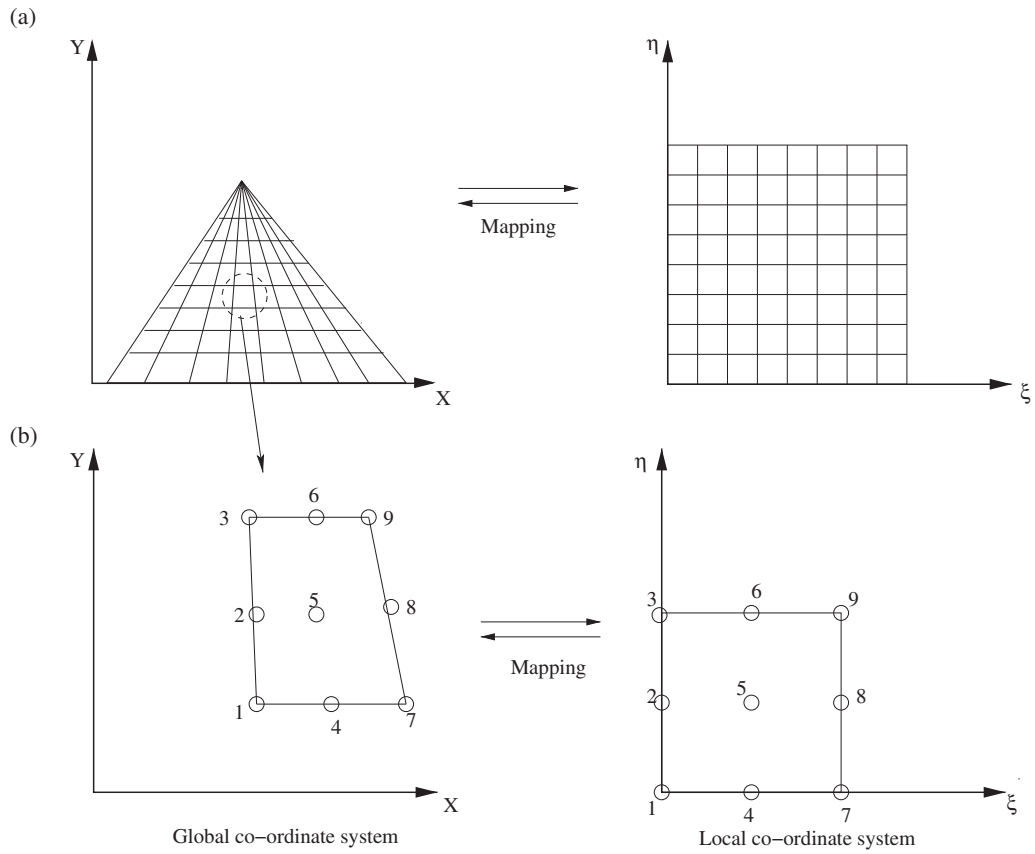


**Fig. 2.** (a) The mapping of lower triangular domain to a square domain in  $\xi$ - $\eta$  coordinate system and (b) the mapping of an individual element to a single element in  $\xi$ - $\eta$  coordinate system.

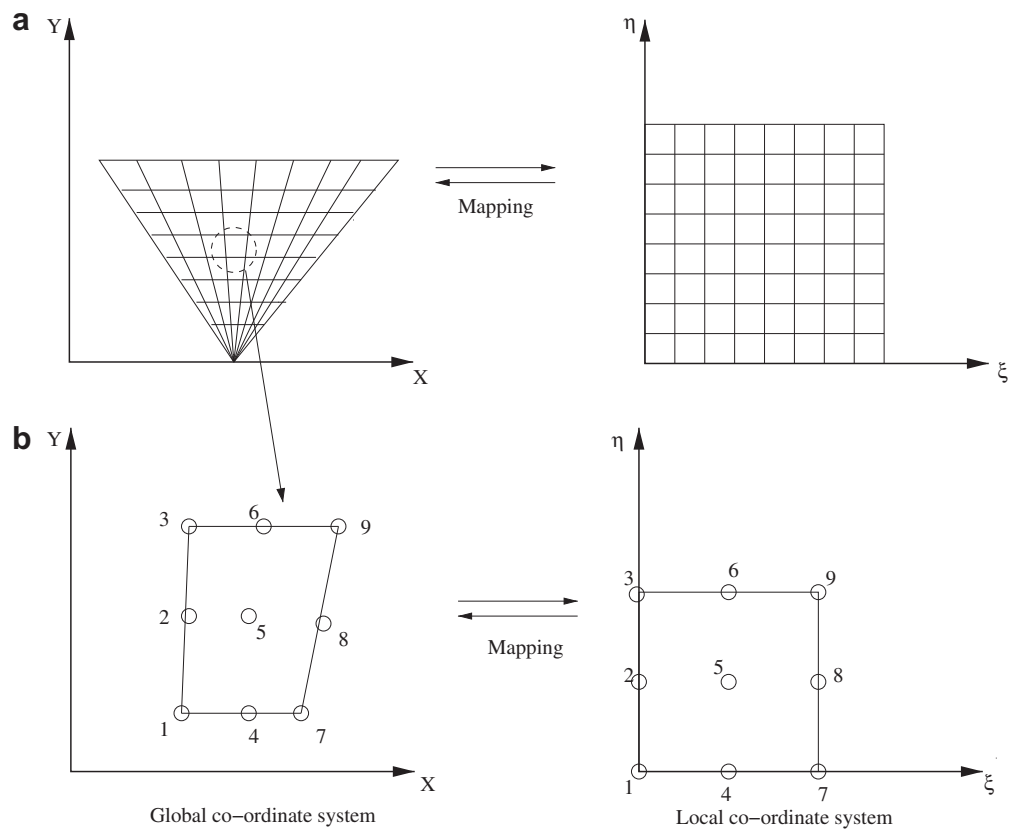


**Fig. 3.** (a) The mapping of upper triangular domain to a square domain in  $\xi$ - $\eta$  coordinate system and (b) the mapping of an individual element to a single element in  $\xi$ - $\eta$  coordinate system.

(a) Entrapped lower triangle ( $\triangle ABC$ )

$$\Pi = \sqrt{2} \overline{Nu}_l \quad \text{at } X = 0, \quad Y = 0, \quad (23)$$

$$\Pi = 0 \quad \text{at } X = 1, \quad Y = 1, \quad (24)$$

and

$$\Pi = -\sqrt{2} \overline{Nu}_r \quad \text{at } X = 2, \quad Y = 0. \quad (25)$$

(b) Entrapped upper triangle ( $\triangle BDE$ )

$$\Pi = -\sqrt{2} \overline{Nu}_l \quad \text{at } X = 0, \quad Y = 2, \quad (26)$$

$$\Pi = 0 \quad \text{at } X = 1, \quad Y = 1, \quad (27)$$

and

$$\Pi = \sqrt{2} \overline{Nu}_r \quad \text{at } X = 2, \quad Y = 2. \quad (28)$$

The heat transfer coefficient in terms of local Nusselt number ( $Nu$ ) is defined by

$$Nu = -\frac{\partial \theta}{\partial n}. \quad (29)$$

Here  $n$  denotes the outward normal direction of the plane. The local Nusselt numbers at horizontal wall ( $Nu_h$ ), left wall ( $Nu_l$ ) and right wall ( $Nu_r$ ) are defined as follows:

(a) Entrapped lower triangle ( $\triangle ABC$ )

$$Nu_h = \sum_{i=1}^9 \theta_i \frac{\partial \Phi_i}{\partial Y}, \quad (30)$$

$$Nu_l = \sum_{i=1}^9 \theta_i \left( \frac{1}{\sqrt{2}} \frac{\partial \Phi_i}{\partial X} - \frac{1}{\sqrt{2}} \frac{\partial \Phi_i}{\partial Y} \right), \quad (31)$$

and

$$Nu_r = \sum_{i=1}^9 \theta_i \left( -\frac{1}{\sqrt{2}} \frac{\partial \Phi_i}{\partial X} - \frac{1}{\sqrt{2}} \frac{\partial \Phi_i}{\partial Y} \right). \quad (32)$$

(b) Entrapped upper triangle ( $\triangle BDE$ )

$$Nu_h = -\sum_{i=1}^9 \theta_i \frac{\partial \Phi_i}{\partial Y}, \quad (33)$$

$$Nu_l = \sum_{i=1}^9 \theta_i \left( \frac{1}{\sqrt{2}} \frac{\partial \Phi_i}{\partial X} + \frac{1}{\sqrt{2}} \frac{\partial \Phi_i}{\partial Y} \right), \quad (34)$$

and

$$Nu_r = \sum_{i=1}^9 \theta_i \left( -\frac{1}{\sqrt{2}} \frac{\partial \Phi_i}{\partial X} + \frac{1}{\sqrt{2}} \frac{\partial \Phi_i}{\partial Y} \right). \quad (35)$$

The average Nusselt numbers at the horizontal and side walls are

$$\overline{Nu}_h = \frac{\int_0^2 Nu_h dX}{\int_0^2 dX} = \frac{1}{2} \int_0^2 Nu_h dX \quad (36)$$

and

$$\overline{Nu}_l = \overline{Nu}_r = \frac{1}{\sqrt{2}} \int_0^{\sqrt{2}} Nu_l dS. \quad (37)$$

Here  $dS$  denotes the elemental length along inclined sides of the triangular cavity.

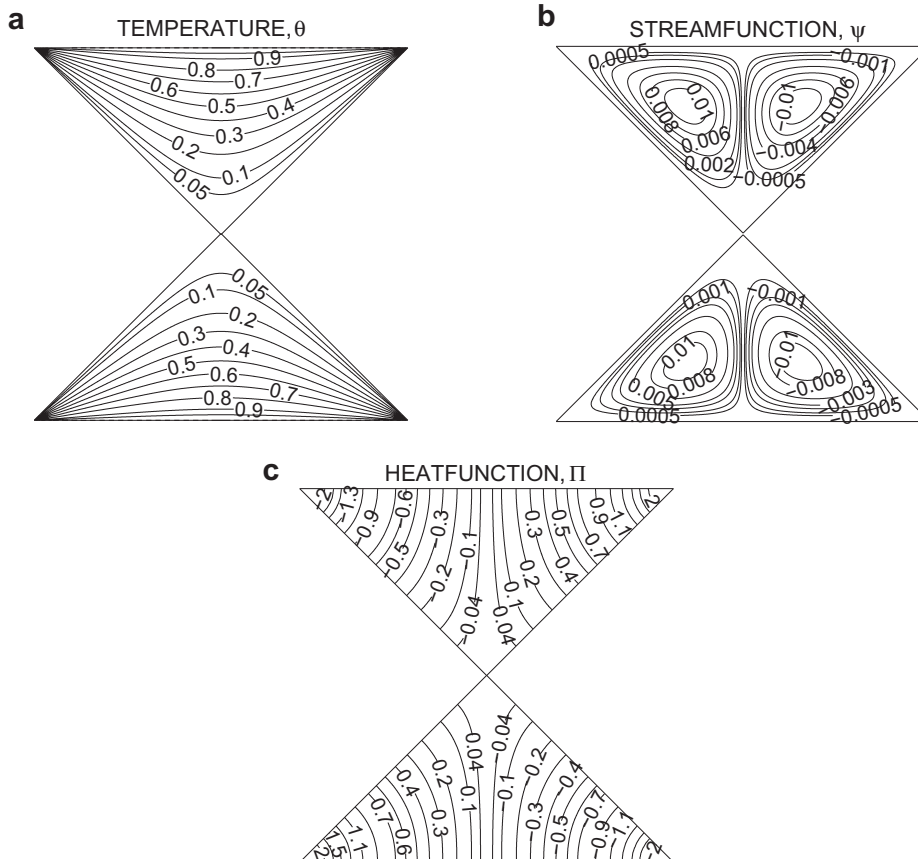


Fig. 4. (a) Temperature ( $\theta$ ), (b) streamfunction ( $\psi$ ) and (c) heatfunction ( $\Pi$ ) contours for uniform heating with  $Pr = 0.015$  and  $Ra = 10^2$ . Clockwise and anti-clockwise flows are shown via negative and positive signs of streamfunctions and heatfunctions, respectively.

3. Results and discussion

3.1. Numerical tests

The computational domain in  $\xi-\eta$  coordinates (see Appendix A) consists of  $20 \times 20$  bi-quadratic elements which correspond to  $41 \times 41$  grid points. It may be noted that, the computational grid in the triangular domain is generated via mapping the lower/upper triangular domain into square domain in  $\xi-\eta$  coordinate system as shown in Figs. 2 and 3 and the procedure is outlined in Appendix A. The bi-quadratic elements with lesser number of nodes smoothly capture the non-linear variations of the field variables which are in contrast with finite difference/finite volume solutions available in the literature. Present simulation studies on isotherms and streamlines on each individual triangular cavity have been compared with earlier simulation results for a specific triangular domain [41] and the results are in good agreement.

In the current investigation, Gaussian quadrature based finite element method provides the smooth solutions at the interior domain including the corner regions as evaluation of residuals depends on the interior Gauss points and thus the effect of corner nodes are less profound in the final solution. In general, the Nusselt numbers for finite difference/finite volume based methods are calculated at any surface using some interpolation functions which are avoided in the current work. The present finite element method based approach offers special advantages on evaluation of local Nusselt numbers at the left, right and top walls as the element basis functions have been used to evaluate the heat flux.

In the present study, Prandtl number is varied from 0.015 to 1000 covering wide range of applications. Also, influence of natural

convection in each triangular cavity has been studied via varying Rayleigh number within  $10^2-10^5$ . Variation of Nusselt number with distance for various Rayleigh numbers as well as variation for average Nusselt number vs. Rayleigh number has been shown to illustrate heat transfer rates within each triangular cavity. Detailed explanations are given in succeeding sections.

3.2. Isotherms, streamlines and heatlines

Figs. 4–8 display the streamlines, isotherms and heatlines for various values of  $Pr$  ( $0.015 \leq Pr \leq 1000$ ) and  $Ra$  ( $10^2 \leq Ra \leq 10^5$ ) within the global system consisting of two triangular cavities attached with each other and each cavity involves cold inclined walls and horizontal hot walls. Based on the physical system, some of the common observations are given as follows. Due to the difference in the temperature of fluid near the horizontal wall, hot fluid moves towards the cold wall, forming two oppositely circulating flows in the system with the eye of the vortices located at the center of each half of the triangular cavity. The thermal transport within triangular cavities is analyzed via heat flow with heatlines. It may be noted that the two corners on horizontal plane have infinite heat flux as the cold wall is directly in contact with the hot inclined walls.

For  $Ra = 10^2$  and  $Pr = 0.015$  (Fig. 4), there is a striking similarity between the heating patterns in both the triangles. It is interesting to observe that the isotherms, streamlines and heatlines within cavities are mirror images of each other and the isotherms are smooth, monotonic curves symmetric to the central axis. The smooth symmetric isotherms and streamlines thus illustrate the insignificant role of gravity towards the flow and heat transfer in

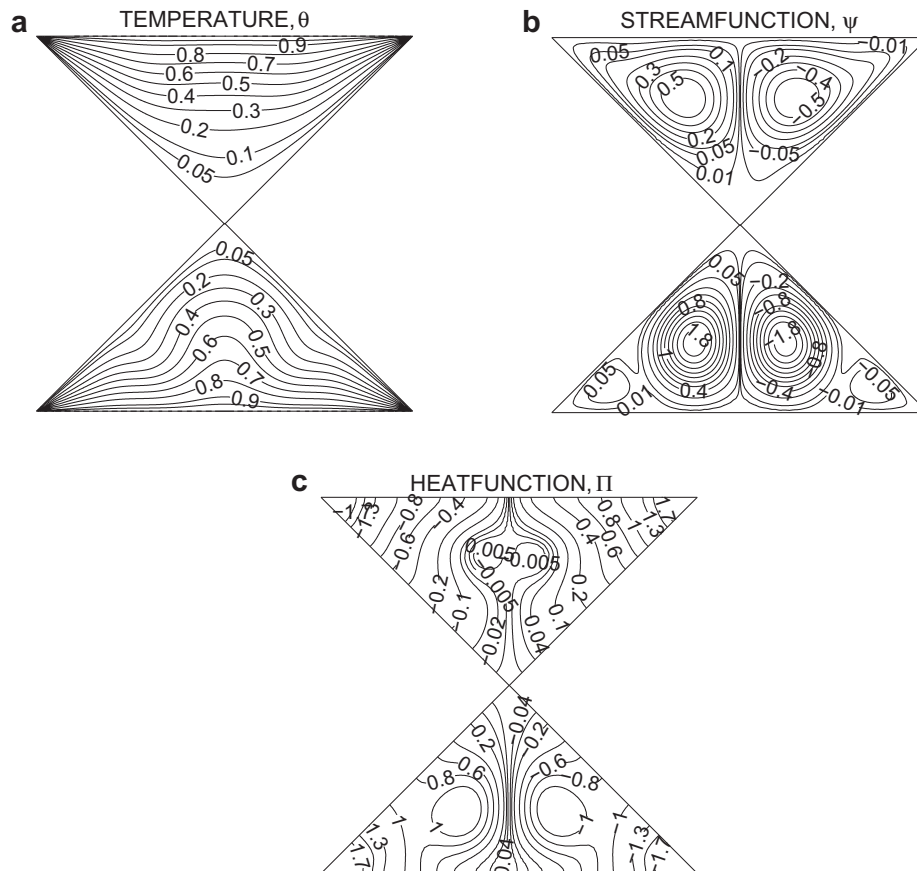


Fig. 5. (a) Temperature ( $\theta$ ), (b) streamfunction ( $\psi$ ) and (c) heatfunction ( $\Pi$ ) contours for uniform heating with  $Pr = 0.015$  and  $Ra = 10^4$ . Clockwise and anti-clockwise flows are shown via negative and positive signs of streamfunctions and heatfunctions, respectively.

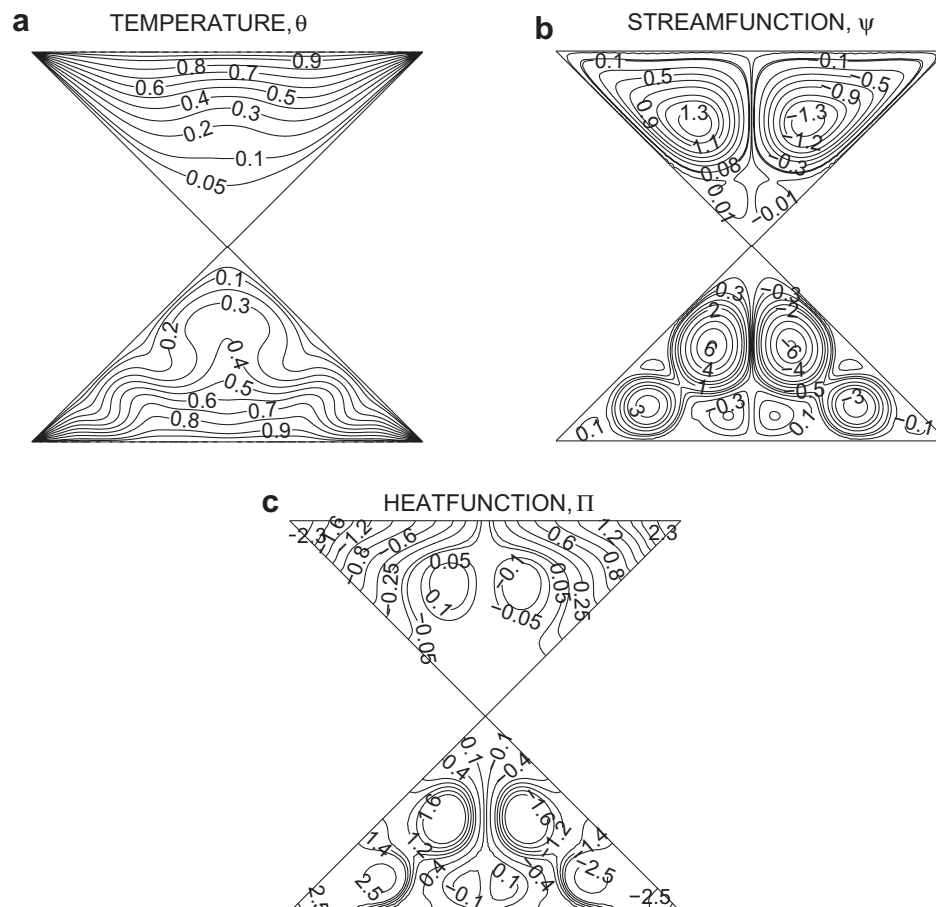
cavities, which further denote that the heat transfer is primarily due to conduction. The heatlines are smooth and it is observed that the lines are perfectly perpendicular to the isotherm lines and the walls. This further indicates that the heat flow is conduction dominant. An important point to note is that the heatlines with greater strength are clustered around the intersection point between horizontal and inclined walls and as we move along the inclined wall, the strength of heatline goes to as low as 0.04 at the common vertex of each triangle. This means that major amount of heat flux or transport occurs near the junction of the hot and cold walls. Thus, relatively less heat flow occurs near the cold–cold junction.

As Rayleigh number increases to  $10^4$  (Fig. 5a–c), interesting features of flow and thermal characteristics have been observed. The isotherms for the upper triangle are smooth and monotonic, but the isotherms are dense near the hot wall. On the other hand, the isotherms are quite dispersed near the bottom corner of the upper triangle. In contrast, for the lower triangle, the isotherms are distorted. The distortion of isotherms near the cold wall as well as at the central regime gradually becomes prominent implying a dominant convection effect. The streamlines in the upper triangle are smooth and monotonic and the magnitude of maximum value of streamfunction ( $|\psi|_{\max}$ ) is found to be 0.5 which signifies that the flow is not intense (Fig. 5b). On the other hand, symmetric primary circulation cells are also observed for the lower triangular cavity and in addition, two secondary cells also appear near the bottom corners. It is observed that  $|\psi|_{\max}$  for the lower triangle is around 1.8 which signifies a larger intensity of convection. The secondary cells are observed due to retarded flow near the bottom corners

and this especially occurs for fluids with small Prandtl number (Fig. 5b).

Finally, the heatlines illustrate that convection dominant effect plays a critical role on larger heat flow from horizontal walls to the top portion of inclined walls especially for the lower triangle (Fig. 5c). Heatlines also show that there is a clear difference in the heat flow trajectory for both the triangles. This difference is largely attributed to the boundary conditions and convection within the system. For the lower triangle, it is observed that the heatlines are less dense near the bottom corner points due to conduction dominant heat transfer. Two symmetric cells of heatlines are observed near the core of the lower triangular cavity and these cells denote convective heat transfer due to circulation of fluid as seen from streamlines at the core. The convective energy transfer facilitates thermal mixing leading to less thermal gradient at the core as the dense heatlines are also observed near the core. The heatlines are also seen to be connected between the top wall to the inclined wall for the upper triangle. Deformation of heatlines near the core is observed, showing the presence of convection in the system. However, the thermal mixing near the core is not intense due to lower heat flow for the upper triangle as seen in Fig. 5c. It may be noted that the magnitudes of heatfunction at the core is 1 for the lower triangle whereas it is around 0.005 for the upper triangle. Overall, larger heat may be recovered within the lower cavity for fluids with smaller  $Pr$  at  $Ra = 10^4$ .

As Rayleigh number increases to  $10^5$  for  $Pr = 0.015$  (Fig. 6a–c), stronger and multiple circulation cells in flow and heat transfer are observed for the lower triangle. It is seen that the isotherms



are highly deformed in the lower triangle (Fig. 6a). In addition, isotherms exhibit oscillations and compressions near the bottom wall and also at the intermediate locations of side walls. These oscillations are due to multiple circulation cells in the cavity. On the other hand, the isotherms are similar to the previous cases but are suppressed towards the horizontal wall for the upper triangle. It may be noted that the magnitude of streamfunctions are larger for  $Ra = 10^5$  signifying the larger intensity of circulations. Multiple flow circulations greatly influence the heatline patterns and heat energy distributions as seen in Fig. 6b and c. Similar to the previous cases, the lower triangle clearly shows higher magnitude for heat transfer due to convective circulations compared to upper triangular cavity as seen from the heatfunction magnitudes. Different convective circulation cells are observed for heatlines near the core and this illustrates a larger magnitude of convective heat transfer which is also seen from heatline contours for the lower triangle. In contrast, a single convection cell of  $|II|_{\max} = 0.1$  is observed for the upper triangle. The top portion of the inclined wall receives most of the heat from the hot wall. But, the presence of convective cells does not contribute to higher heat transfer compared to the lower triangle which has  $|II|_{\max} = 1.6$ . Overall, the lower triangular enclosure has higher heat recovery capacity for  $Ra = 10^5$  for fluids with low  $Pr$ .

Next, the effect of a change in the Prandtl numbers for higher Rayleigh number ( $Ra = 10^5$ ) is analyzed. Firstly,  $Pr$  is increased to 0.026 (Figure not shown). It was observed that variation of Prandtl number from 0.015 to 0.026 does not enhance the heat transfer in

the upper triangle significantly as the heatlines and streamlines show nearly the same patterns. Influence of  $Pr$  is further investigated for  $Pr = 0.7$  (Fig. 7a–c). It is observed that multiple circulations have been totally suppressed for the lower triangle and there are only single circulation cells each symmetric to the central axis. But, the circulations are highly intense and maximum value of stream function ( $|\psi|_{\max}$ ) is 12 for  $Pr = 0.7$  whereas  $|\psi|_{\max}$  was 6 for  $Pr = 0.026$ . It may be observed that the isotherms are compressed near the horizontal wall and inclined walls whereas the temperature at the core varies within 0.4–0.6 for the lower triangle. The heatlines are dense near the core and are symmetric in the lower triangle. The strong convective heat transport with  $|II|_{\max} = 7$  is seen near the core and identical circulation cells occur for streamlines and heatlines (Fig. 7b and c). On the other hand,  $|II|_{\max} = 1.6$  was observed in the lower triangle for  $Pr = 0.026$ . Therefore, enhanced thermal mixing occurs near the core in the lower triangle. In contrast, the stratification of isotherms is observed in the upper triangle. It may be noted that  $|\psi|_{\max} = 1.6$  in the upper triangle whereas  $|\psi|_{\max}$  was around 1.5 at  $Pr = 0.026$ . It may be noted that, the flow circulation in the upper triangle is only slightly influenced by  $Pr$ . It is observed that, the eyes of the vortices tend to be shifted near the top horizontal wall and thus isotherms are compressed near the top wall in the upper triangle. However, the compression of isotherms is greater in the lower triangle. Similar to the lower triangle, the heatline patterns show a pair of convection cells at the core in the upper triangle. However, the intensity of the convection is found to be smaller in the upper triangle. It may be noted

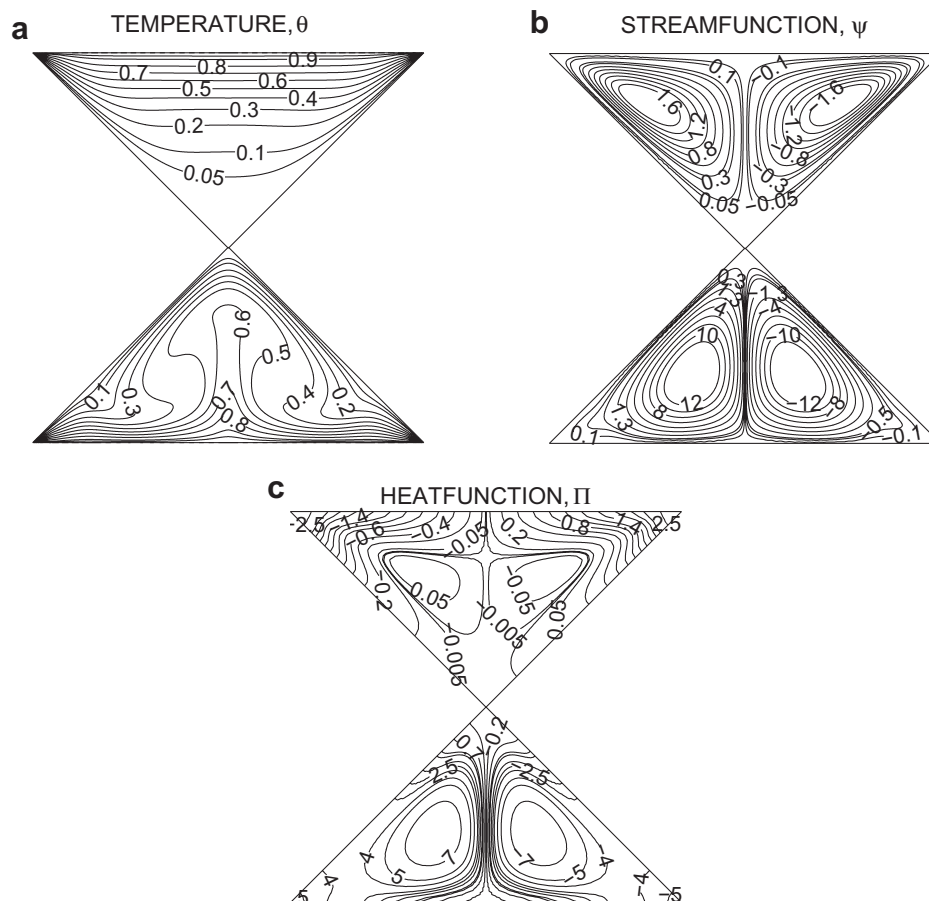


**Fig. 7.** (a) Temperature ( $\theta$ ), (b) streamfunction ( $\psi$ ) and (c) heatfunction ( $II$ ) contours for uniform heating with  $Pr = 0.7$  and  $Ra = 10^5$ . Clockwise and anti-clockwise flows are shown via negative and positive signs of streamfunctions and heatfunctions, respectively.

that at  $|II|_{\max} = 0.05$  at the core for the upper triangle and  $\theta$  at the core varies within 0.1–0.5. As in the previous cases, the intensity of circulation as well as heat transfer is lower in the upper triangle.

Finally, Fig. 8a–c illustrates the profiles for large Prandtl number ( $Pr = 1000$ ) with  $Ra = 10^5$ . The isotherms near the core show a well dispersed pattern with  $\theta = 0.5$ –0.6 for the lower triangle (Fig. 8a) whereas isotherms near the core was found to vary within 0.4–0.6 for  $Pr = 0.7$  (Fig. 7a). Overall, the core is slightly hotter for  $Pr = 1000$  as seen in Fig. 8a. The isotherms in the upper triangle depict a similar pattern as seen for the previous case (Fig. 7a), i.e. the isotherms are stratified with almost no dispersion near the intersection of the cold inclined walls for the upper triangle. Even though isotherms show more uniform thermal mixing near the core for the lower triangle, it is interesting to observe that the streamline patterns for both the cases ( $Pr = 0.7, 1000$ ) are almost identical, i.e.  $|\psi|_{\max} = 12$  for both the cases (Figs. 7b and 8b). Heatlines also exhibit similar trends for  $Pr = 0.7$  and  $Pr = 1000$ . It may be noted that,  $|II|_{\max} = 7$  for  $Pr = 0.7$  and  $Pr = 1000$  for the lower triangle. The dense heatlines from the middle portion of inclined walls as well as along the central symmetric lines are observed for the lower triangle. This signifies intense thermal mixing. Further, a large region near the core is associated with convective heat transfer as seen from the circulation loops. The dense heatlines at the top portion of the inclined walls are also observed in the upper triangle, but overall magnitudes of heatlines are less than those in the lower triangle. As in the previous case, there is a central convection cell with less intensity of heat flow. Thus, it may be inferred that irrespective of the fluid, the upper triangular cavity always exhibits smaller heat transfer rates compared to the lower triangular cavity.

Based on the present analysis, fluids with higher Prandtl number for the lower triangular cavity may be considered efficient to achieve effective heat recovery from the system.

### 3.3. Heat transfer rate: Nusselt numbers

Fig. 9 shows the variation of heat transfer rate ( $Nu_l$ ) vs. distance along the inclined walls of both the triangles. The upper panel of the plot shows the heat transfer rate dissipation of the inverted upper triangle whereas the lower panel of the plot represents the lower triangular domain of the system. As expected, for both the triangles the heat transfer is negligible at the intersection of cold walls and maximum heat transfer occurs at the intersection of cold wall with the hot wall.

The heat transfer rates within both the triangles for various Prandtl numbers have been analyzed. The heat transfer rate ( $Nu_l$ ) for the lower triangle shows a wavy pattern for  $Pr = 0.015$  and  $Ra = 10^5$ . It is also observed that the heat transfer rate is zero initially at the zone of intersection of cold walls. Thereafter, the rate steadily increases till a distance of 0.4 along the inclined wall and then decreases rapidly till the distance of 0.6. Further,  $Nu_l$  increases again with a next maximum value at distance 0.9 and minimum at 1.1. This wavy pattern is attributed to the presence of multiple circulation cells as seen in Fig. 6b. Each circulation cell is characterized by an intense central core region and a less intense outer region. As a result,  $Nu_l$  starts to decrease at the zone of intersection of two circulation cells. This wavy pattern of  $Nu_l$  or  $Nu_r$  is also due to various levels of compression of isotherms resulting from multiple circulation cells. On the other hand, there is no wavy

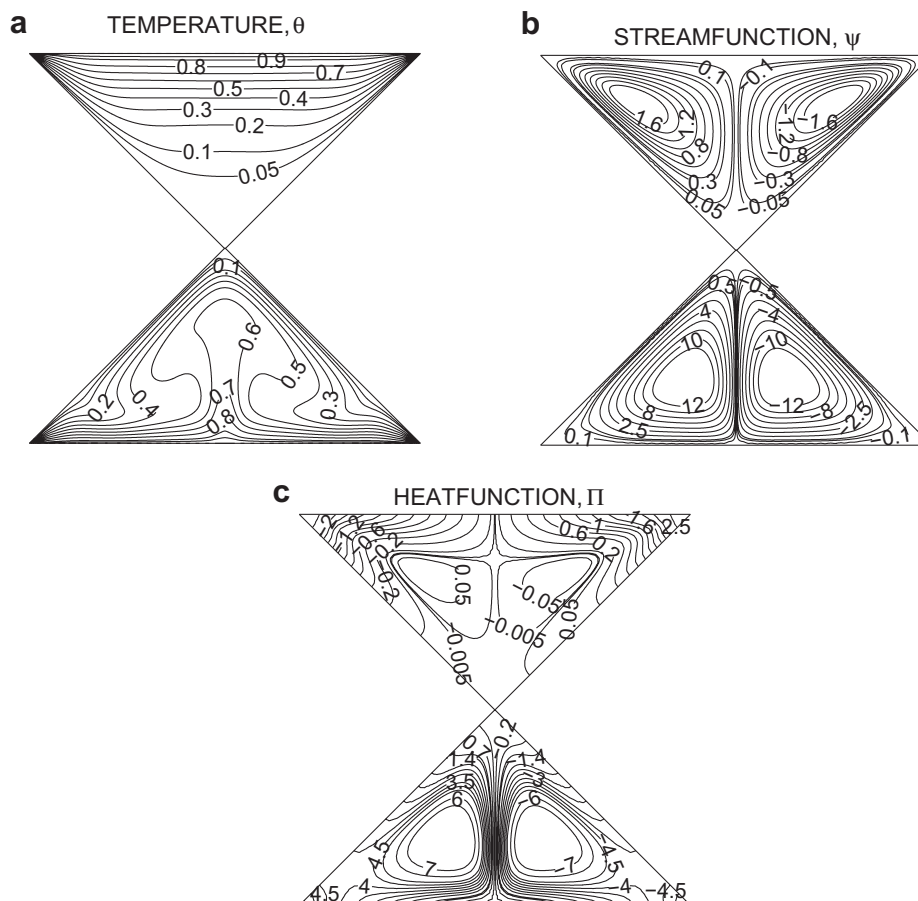
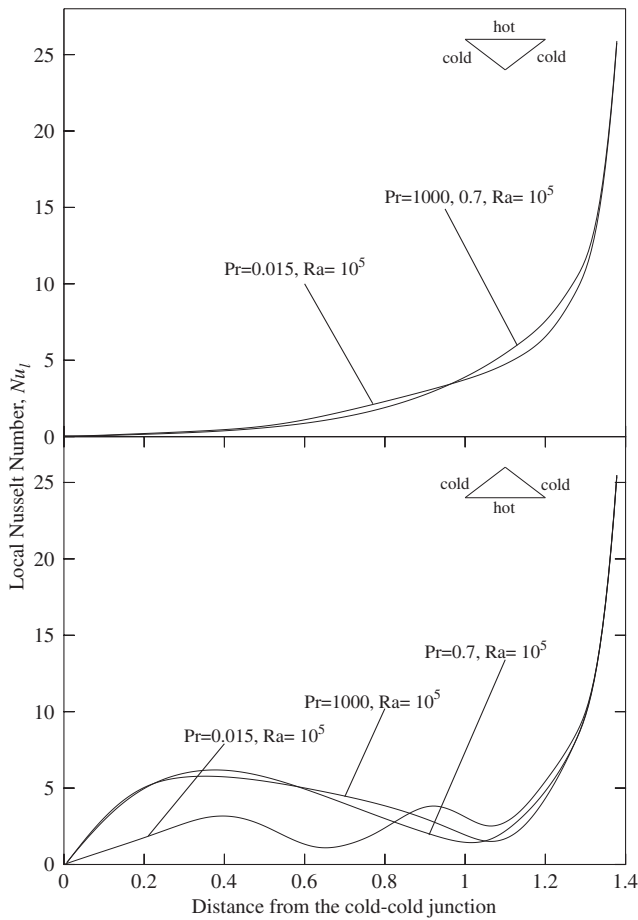


Fig. 8. (a) Temperature ( $\theta$ ), (b) streamfunction ( $\psi$ ) and (c) heatfunction ( $II$ ) contours for uniform heating with  $Pr = 1000$  and  $Ra = 10^5$ . Clockwise and anti-clockwise flows are shown via negative and positive signs of streamfunctions and heatfunctions, respectively.



**Fig. 9.** Variation of local Nusselt numbers with distance along the inclined wall for various  $Pr$  (0.015, 0.7, 1000) for  $Ra = 10^5$ . The inset illustrates the schematic of the computational domain.

pattern observed for  $Nu_l$  or  $Nu_r$  for the upper triangle. The values of heatfunctions numerically increase along the inclined wall towards the hot–cold junction (see Fig. 6) and that results in the increase of  $Nu_l$  along the inclined wall. The oscillatory nature of  $Nu_l$  is further explained based on various zones of dense heatlines along the inclined wall. As expected, infinite heat transfer rate occurs at the junction of intersection of hot and the cold walls.

As the Prandtl number is increased to 0.7 and to 1000 for  $Ra = 10^5$ , the heat transfer rates show almost similar patterns for both the Prandtl numbers. For  $Pr = 0.7$  the heat transfer rate increases till distance of 0.3 for the lower triangle, thereafter that slowly decreases and finally increases rapidly towards the edge. This may be explained based on isotherm distribution. It is observed that the isotherms are highly compressed near the hot–cold junction of the bottom wall and intermediate locations of inclined wall for the lower triangle. The isotherms are also found to be dispersed at a point near the cold–cold junction. Overall, the heat transfer rate ( $Nu_l$ ) is high at the hot–cold junction and  $Nu_l$  also shows oscillations based on various levels of compression of isotherms. The heatlines also illustrate the dense heatlines near the zone of hot–cold junctions and it is observed that the large magnitudes of heatfunction occur near the hot–cold junctions. Therefore,  $Nu_l$  is large near the hot–cold junctions and is very high near the edges. On the other hand,  $Nu_l$  or  $Nu_r$  show almost similar monotonic tendency for all  $Pr$  within the upper triangle. This is due to the fact that the isotherms for upper triangle show similar patterns as convection has little influence. The heatlines are dense near the junctions of hot–cold walls whereas they are dispersed far away

from the hot–cold junction and as a result, the monotonic trend of  $Nu_l$  along the inclined walls is observed for the upper triangle irrespective of  $Pr$ .

Fig. 10 shows the variation of heat transfer along the horizontal walls of upper and lower triangles. For the lower triangle, the general trend is that the heat transfer rate is infinite at the two edges of the horizontal wall. But, along the wall, heat transfer rate decreases till the mid point of the wall and afterwards increases towards the edge. This is due to the presence of a pair of circulatory loops symmetric to the vertical axis (Figs. 7b and 8b). For  $Pr = 0.015$ , it is observed that heat transfer rate has a constant low value between the region  $X = 0.6$  till  $X = 1.4$  which is due to the presence of multiple circulatory loops for the system (Fig. 6b and c). For  $Pr = 0.7$  and 1000, it is observed that the heat transfer rate decreases from the edge towards the center of the horizontal wall. The enhanced thermal mixing results in less thermal gradient near the central region as seen in Figs. 7a and 8a and thus, the heat transfer rate ( $Nu_h$ ) is less near the central region of the bottom wall. Interesting results are observed for heat transfer rates in the upper triangle. Except at the edges the heat transfer rate ( $Nu_h$ ) is very low along the top wall for all Prandtl numbers. The heatlines are much denser near the hot–cold junctions and the magnitudes of heatfunctions are also larger near the hot–cold junctions whereas the values of heatfunctions are smaller near the center. The heatlines are also dispersed near the central region of the horizontal wall. This explains monotonic trend of  $Nu_h$  along each half of the upper triangle.

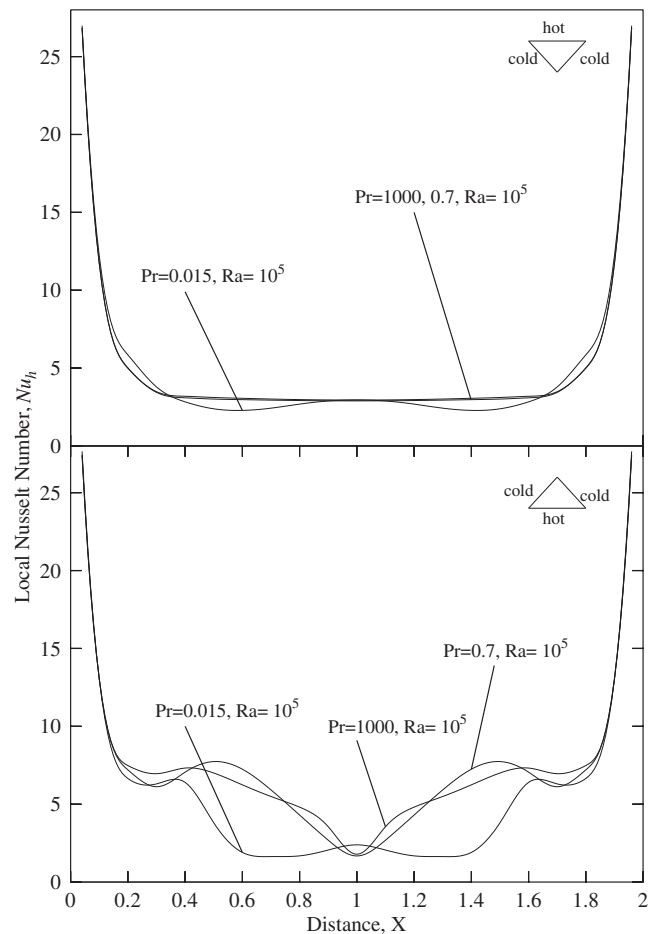


**Fig. 10.** Variation of local Nusselt numbers with distance along the horizontal wall for various  $Pr$  (0.015, 0.7, 1000) for  $Ra = 10^5$ . The inset illustrates the schematic of the computational domain.

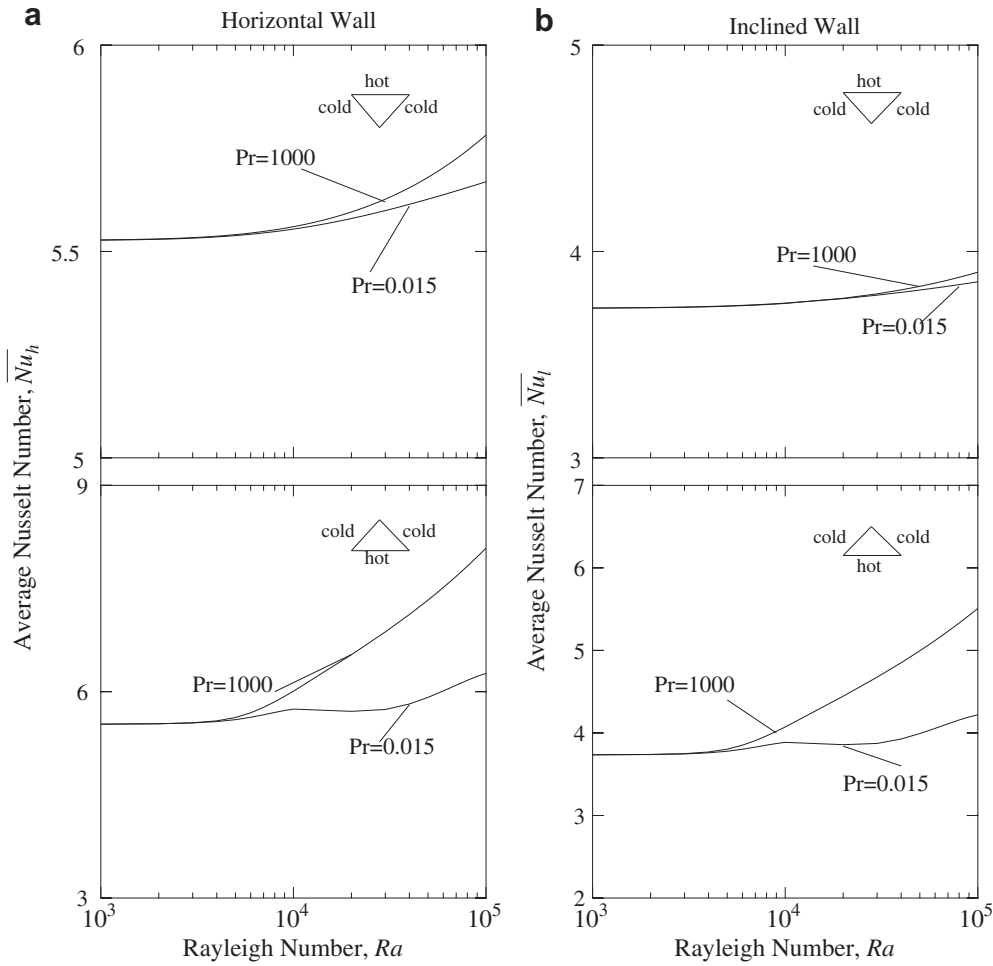


Fig. 11. Variation of average Nusselt number with Rayleigh number for (a) horizontal wall and (b) inclined wall for  $Pr = 0.015$  and  $1000$ . The inset illustrates the schematic of the computational domain.

Fig. 11a and b shows the distributions of the average Nusselt number for horizontal and inclined walls, respectively, vs. the logarithmic Rayleigh number. The general trend is that the average Nusselt number increases with Rayleigh numbers. Fig. 11a illustrates that the average Nusselt number remains almost constant till around  $Ra = 8 \times 10^3$  for  $Pr = 1000$  in the lower triangle. Afterwards, the average Nusselt number for  $Pr = 1000$  increases rapidly whereas for  $Pr = 0.015$ , the average Nusselt number does increase but rate of the increase is small and remains nearly constant till  $Ra = 4 \times 10^4$  (see lower panel of Fig. 11a). The smaller variation for  $\overline{Nu}_h$  is due to secondary and multiple circulations and heat transfer with  $Pr = 0.015$  (Fig. 6) compared to single symmetric highly intense circulation with  $Pr = 1000$  (see Fig. 8). Similar pattern is observed in lower panel of Fig. 11b for the inclined walls. The upper panels of Fig. 11a and b show the monotonic increase, but a slower rate for  $\overline{Nu}_h$  and  $\overline{Nu}_l$  with  $Ra$  in the upper triangle. Based on thermal equilibrium, the average Nusselt number of the horizontal wall is found as  $\sqrt{2}$  times that of the inclined wall. This result is well matched in all cases confirming the thermal equilibrium of the system. A correlation has been developed for a generalized relationship between  $\overline{Nu}_h$  or  $\overline{Nu}_l$  and  $Ra$  in a convection dominant regime. A correlation for  $Nu_h$  or  $Nu_l$  and  $Ra$  was found for  $Pr = 1000$ . The critical  $Ra$  is observed as  $4 \times 10^4$  for  $Pr = 1000$  for the upper triangle and that implies that convection is significant for  $Ra \geq Ra_c$  and the following correlation is obtained for the upper triangle:

$$\overline{Nu}_h = \sqrt{2} \overline{Nu}_l = 4.3613 Ra^{0.024}, \quad Pr = 1000, \quad Ra \geq 4 \times 10^4. \quad (38)$$

Correlations have also been obtained for the lower triangle. As expected from the physical situation (Fig. 11a and b), the critical Rayleigh number  $Ra_c$  is found to be  $8 \times 10^3$  for  $Pr = 1000$ . This implies that for  $Ra \geq 8 \times 10^3$ , convection is significant and the following correlation is obtained for the lower triangle:

$$\overline{Nu}_h = \sqrt{2} \overline{Nu}_l = 1.8628 Ra^{0.13}, \quad Pr = 1000, \quad Ra \geq 8 \times 10^3. \quad (39)$$

It may be noted that, the power law correlation is not presented for  $Pr = 0.015$ , as an inflexion point for  $\overline{Nu}_h$  and  $\overline{Nu}_l$  is observed in the lower triangle.

#### 4. Conclusion

The objective of the present study is to establish a physical as well as computational insight into the heat flow in natural convection within a complex enclosure for hot material processing applications. The system comprises of entrapped fluid in two triangular cavities formed between a pair of adjacent square tubes normally seen in heat recovery systems.

The key parameters used for the analysis are Rayleigh number, Prandtl number and Nusselt number. The motivation was to

examine the heat transfer to the entrapped fluid in the system commonly used for practical applications in heat recovery during hot material processing. In addition, the values of Prandtl numbers have been chosen such that the system depicts a wide range of commonly used applications. The visualization of heat flow inside the cavity has been carried out based on the heatlines concept in the triangular cavity, which provides knowledge of the heat flow trajectory. The conduction dominant heat transport is observed at  $Ra = 10^2$  for  $Pr = 0.015$ . However, as  $Ra$  increases to  $10^4$ , convection begins, and the primary circulation cells get distorted with initiation of secondary circulation cells in the lower triangle. The strong dominance of convection in heat transfer is clearly illustrated by large magnitudes of streamfunctions and heatfunctions when  $Ra$  is increased to  $10^5$ . As  $Pr$  increases, multiple circulations are still observed in the lower triangle and flow becomes gradually intense. Heat transport is mainly due to convection in multiple circulation zones and thus multiple cells in heatline contours are also observed for  $Pr = 0.015$  and  $Pr = 0.026$ . It is observed that multiple circulations are suppressed for  $Pr \geq 0.7$  and dense heatlines are observed near the bottom portion of inclined walls in the lower triangular cavity. It is observed that the heat transfer of the central region is dominated by convection as seen from the heatlines. Thus, enhanced thermal mixing occurs near the core at higher  $Pr$ .

On the other hand, in the upper triangle, there is almost no effect of change in Prandtl number on the heat transfer pattern of the fluid even though a convection cell at the core is observed. Further, the heat transfer rates are very low throughout the system irrespective of the  $Pr$  in the cavity. Thus, it may be concluded that for high heat transfer, higher Prandtl number fluids may be used in the lower triangular cavity and for the upper triangular cavity any fluid can be chosen as  $Pr$  does not affect the heating pattern. The enhanced heat transfer in the upper triangle may be carried out with forced convection which is beyond the scope of the present study.

Nusselt numbers are quite large at the intersection of inclined and top walls due to infinite heat transfer rate for both the upper and lower triangles. For the lower triangle, multiple circulations contribute to the wavy pattern of Nusselt number for low Prandtl numbers indicating fluctuating magnitudes of heat transfer rates at various locations along the inclined and top wall. The wavy pattern in spatial distribution of Nusselt numbers gradually disappears as  $Pr$  increases. On the contrary, the isotherm and heatline patterns remain almost identical irrespective of the Prandtl number in the upper triangle. Correlations have been developed for  $Pr = 1000$  in upper and the lower triangle to illustrate convective heat transfer rates and a critical  $Ra$  is obtained to delineate the conduction dominant zone.

## Appendix A

The name iso-parametric derives from the fact that the same parametric function describing the geometry may be used for interpolating spatial variable within an element. Figs. 2 and 3 show the grid generation for  $(x, y)$  and  $(\xi, \eta)$  coordinates via following mapping relationships:

$$X = \sum_{k=1}^9 \Phi_k(\xi, \eta) x_k,$$

$$Y = \sum_{k=1}^9 \Phi_k(\xi, \eta) y_k.$$

Here  $(x_k, y_k)$  are the  $X, Y$ -coordinates of the  $k$  nodal points as seen in Figs. 2 and 3 and  $\Phi_k(\xi, \eta)$  is the basis function. The nine basis functions are:

$$\Phi_1 = (1 - 3\xi + 2\xi^2)(1 - 3\eta + 2\eta^2),$$

$$\Phi_2 = (1 - 3\xi + 2\xi^2)(4\eta - 4\eta^2),$$

$$\Phi_3 = (1 - 3\xi + 2\xi^2)(-\eta + 2\eta^2),$$

$$\Phi_4 = (4\xi - 4\xi^2)(1 - 3\eta + 2\eta^2),$$

$$\Phi_5 = (4\xi - 4\xi^2)(4\eta - 4\eta^2),$$

$$\Phi_6 = (4\xi - 4\xi^2)(-\eta + 2\eta^2),$$

$$\Phi_7 = (-\xi + 2\xi^2)(1 - 3\eta + 2\eta^2),$$

$$\Phi_8 = (-\xi + 2\xi^2)(4\eta - 4\eta^2),$$

$$\Phi_9 = (-\xi + 2\xi^2)(-\eta + 2\eta^2).$$

The above basis functions are used for mapping the triangular domain or elements within the triangle into square domain and the evaluation of integrals of residuals.

## References

- [1] K.A. Joudi, I.A. Hussein, A.A. Farhan, Computational model for a prism shaped storage solar collector with a right triangular cross section, *Energy Conservat. Manage.* 45 (3) (2004) 391–409.
- [2] C. Lei, J.C. Patterson, Natural convection in a reservoir sidearm subject to solar radiation: experimental observations, *Exp. Fluids* 32 (2002) 590–599.
- [3] A. Omri, J. Orfi, S. Ben Nasrallah, Natural convection effects in solar stills, *Desalination* 183 (1–3) (2005) 173–178.
- [4] E. Boridy, Potential flow past an open spherical cavity, *J. Appl. Phys.* 67 (11) (1990) 6687–6693.
- [5] J. Ulir, Chemistry and technology of molten salts reactors – history and perspectives, *J. Nucl. Mater.* 360 (2007) 6–11.
- [6] M. Bahador, B. Sunden, Investigation on the effects of fly ash particles on the thermal radiation in biomass fired boilers, *Int. J. Heat Mass Transfer* 51 (9–10) (2008) 2411–2417.
- [7] H.X. Wang, K. Cheng, X. Chen, W.X. Pan, Three-dimensional modeling of heat transfer and fluid flow in laminar-plasma material re-melting processing, *Int. J. Heat Mass Transfer* 49 (13–14) (2006) 2254–2264.
- [8] A.A. Mohamad, J. Sicard, R. Bennacer, Natural convection in enclosures with floor cooling subjected to a heated vertical wall, *Int. J. Heat Mass Transfer* 49 (1–2) (2006) 108–121.
- [9] C.C. Yao, B.T.F. Chung, G.X. Wang, Mushy zone equilibrium solidification of a semitransparent layer subject to radiative and convective cooling, *Int. J. Heat Mass Transfer* 45 (11) (2002) 2397–2405.
- [10] H. Zhang, X.Y. Wang, L.L. Zheng, X.Y. Jiang, Studies of splat morphology and rapid solidification during thermal spraying, *Int. J. Heat Mass Transfer* 44 (24) (2001) 4579–4592.
- [11] V. Lamaison, Y. Scudeller, J.P. Bardou, F. Danes, S.W. Peng, J.P. Dory, Experimental study of transfer phenomena during drying of paint film under infrared heating, *Int. J. Therm. Sci.* 40 (2) (2001) 181–194.
- [12] H. Liu, E.J. Lavernia, R.H. Rangel, An analysis of freeze-up phenomena during gas atomization of metals, *Int. J. Heat Mass Transfer* 38 (12) (1995) 2183–2193.
- [13] S.U. Rahman, Natural convection along vertical wavy surfaces: an experimental study, *Chem. Eng. J.* 84 (3) (2001) 587–591.
- [14] Y. Yamanaka, K. Kakimoto, H. Ozoe, S.W. Churchill, Rayleigh–Benard oscillatory natural convection of liquid gallium heated from below, *Chem. Eng. J.* 71 (3) (1998) 201–205.
- [15] S.G. Akterian, K.A. Fikiin, Numerical simulation of unsteady heat conduction in arbitrary shaped canned foods during sterilization processes, *J. Food Eng.* 21 (1994) 343–354.
- [16] A. Jung, P.J. Fryer, Optimising the quality of safe food: computational modelling of a continuous sterilisation process, *Chem. Eng. Sci.* 54 (1999) 717–730.
- [17] S. Wang, S.D. Wang, Distribution optimization for plate-fin catalytic combustion heat exchanger, *Chem. Eng. J.* 131 (1–3) (2007) 171–179.
- [18] H. Ogura, T. Yamamoto, H. Kage, Y. Matsuno, A.S. Mujumdar, Effects of heat exchange condition on hot air production by a chemical heat pump dryer using  $\text{CaO}/\text{H}_2\text{O}/\text{Ca}(\text{OH})_2$  reaction, *Chem. Eng. J.* 86 (1–2) (2002) 3–10.
- [19] L. Magistri, A. Traverso, A.F. Massardo, Heat exchangers for fuel cell and hybrid system applications, *J. Fuel Cell Sci. Technol.* 3 (2) (2006) 111–118.
- [20] J. Kragh, J. Rose, T.R. Nielsen, S. Svendsen, New counter flow heat exchanger designed for ventilation systems in cold climates, *Energy Build.* 39 (11) (2007) 1151–1158.
- [21] A.K. Gholap, J.A. Khan, Design and multi-objective optimization of heat exchangers for refrigerators, *Appl. Energy* 84 (12) (2007) 1226–1239.
- [22] R. Fan, Y.Q. Jiang, Y. Yao, D. Shiming, Z.L. Ma, A study on the performance of a geothermal heat exchanger under coupled heat conduction and groundwater advection, *Energy* 32 (11) (2007) 2199–2209.
- [23] B.M. Burnside, N.F. Shire, Heat transfer in flow boiling over a bundle of horizontal tubes, *Chem. Eng. Res. Des.* 83 (A5) (2005) 527–538.
- [24] Z.F. Sun, C.G. Carrington, J.A. Anderson, Q. Sun, Air flow patterns in dehumidifier wood drying kilns, *Chem. Eng. Res. Des.* 82 (A10) (2004) 1344–1352.

- [25] S. Maamir, B. Zeghami, A. Hadjadj, D. Rondot, Influence of vaporization by a water reservoir on flows through a corrugated duct, *Can. J. Chem. Eng.* 78 (2) (2000) 293–303.
- [26] M.H.I. Baird, B.A. Legree, Natural convective heat-transfer from open vertical tubes, *Can. J. Chem. Eng.* 72 (4) (1994) 755–758.
- [27] I. Nirdosh, G.H. Sedahmed, Natural-convection mass-transfer inside horizontal square ducts, *Chem. Eng. Commun.* 130 (1994) 193–201.
- [28] H. Salmun, Convection patterns in a triangular domain, *Int. J. Heat Mass Transfer* 38 (2) (1995) 351–362.
- [29] Yu. E. Karyakin, Yu. A. Sokovishin, O.G. Martynenko, Transient natural convection in triangular enclosures, *Int. J. Heat Mass Transfer* 31 (1988) 1759–1766.
- [30] E.M. Del Campo, M. Sen, E. Ramos, Analysis of laminar natural convection in a triangular enclosure, *Int. J. Heat Mass Transfer* 13 (1988) 353–372.
- [31] X.B. Wu, K. Kakimoto, H. Ozoe, Z.Y. Guo, Numerical study of natural convection in Czochralski crystallization, *Chem. Eng. J.* 71 (3) (1998) 183–189.
- [32] E.H. Ridouane, A. Campo, M. Hasnaoui, Turbulent natural convection in an air-filled isosceles triangular enclosure, *Int. J. Heat Fluid Flow* 27 (3) (2006) 476–489.
- [33] E.H. Ridouane, A. Campo, Formation of a pitchfork bifurcation in thermal convection flow inside an isosceles triangular cavity, *Phys. Fluids* 18 (7) (2006) 07410.
- [34] A. Ben-Nakhi, M.A. Mahmoud, Conjugate natural convection in the roof cavity of heavy construction building during summer, *Appl. Therm. Eng.* 27 (2–3) (2007) 287–298.
- [35] Y. Varol, A. Koca, H.F. Oztop, Natural convection in a triangle enclosure with flush mounted heater on the wall, *Int. Commun. Heat Mass Transfer* 33 (8) (2006) 951–958.
- [36] Y. Varol, H.F. Oztop, A. Varol, Natural convection in porous triangular enclosures with a solid adiabatic fin attached to the horizontal wall, *Int. Commun. Heat Mass Transfer* 34 (1) (2007) 19–27.
- [37] E.F. Kent, E. Asmaz, S. Ozerbay, Laminar natural convection in right triangular enclosures, *Heat Mass Transfer* 44 (2) (2007) 187–200.
- [38] A. Omri, M. Najjari, S. Ben Nasrallah, Numerical analysis of natural buoyancy-induced regimes in isosceles triangular cavities, *Numer. Heat Transfer Part A: Appl.* 52 (7) (2007) 327–341.
- [39] A. Koca, H.F. Oztop, Y. Varol, The effects of Prandtl number on natural convection in triangular enclosures with localized heating from below, *Int. Commun. Heat Mass Transfer* 34 (4) (2007) 511–519.
- [40] A. Campo, E.H. Ridouane, Enhancement of natural convection transport in slender right-angled triangular cavities by way of molding the upper insulated wall, *J. Enhanced Heat Transfer* 12 (4) (2005) 327–341.
- [41] H. Asan, L. Namli, Numerical simulation of buoyant flow in a roof of triangular cross section under winter day boundary conditions, *Energy Build.* 33 (2001) 753–757.
- [42] S. Kimura, A. Bejan, The heatline visualization of convective heat-transfer, *J. Heat Transfer-Trans. ASME* 105 (4) (1983) 916–919.
- [43] A. Bejan, *Convection Heat Transfer*, Wiley, New York, 1984.
- [44] F.L. Bello-Ochende, A heat function formulation for thermal convection in a square cavity, *Int. Commun. Heat Mass Transfer* 15 (1988) 193–202.
- [45] V.A.F. Costa, Unification of the streamline, heatline and massline methods for the visualization of two-dimensional transport phenomena, *Int. J. Heat Mass Transfer* 42 (1) (1999) 27–33.
- [46] V.A.F. Costa, Heatline and massline visualization of laminar natural convection boundary layers near a vertical wall, *Int. J. Heat Mass Transfer* 43 (20) (2000) 3765–3774.
- [47] V.A.F. Costa, Unified streamline, heatline and massline methods for the visualization of two-dimensional heat and mass transfer in anisotropic media, *Int. J. Heat Mass Transfer* 46 (8) (2003) 1309–1320.
- [48] V.A.F. Costa, Bejan's heatlines and masslines for convection visualization and analysis, *Appl. Mech. Rev.* 59 (3) (2006) 126–145.
- [49] A. Mukhopadhyay, X. Qin, S.K. Aggarwal, I.K. Puri, On extension of heatline and massline concepts to reacting flows through use of conserved scalars, *J. Heat Transfer-Trans. ASME* 124 (4) (2002) 791–799.
- [50] A. Dalal, M.K. Das, Heatline method for the visualization of natural convection in a complicated cavity, *Int. J. Heat Mass Transfer* 51 (1–2) (2008) 263–272.
- [51] Q.H. Deng, G.F. Tang, Numerical visualization of mass and heat transport for conjugate natural convection/heat conduction by streamline and heatline, *Int. J. Heat Mass Transfer* 45 (11) (2002) 2373–2385.
- [52] T. Basak, S. Roy, A.R. Balakrishnan, Effects of thermal boundary conditions on natural convection flows within a square cavity, *Int. J. Heat Mass Transfer* 49 (23–24) (2006) 4525–4535.
- [53] M.M. Ganzarolli, L.F. Milanez, Natural-convection in rectangular enclosures heated from below and symmetrically cooled from the sides, *Int. J. Heat Mass Transfer* 38 (6) (1995) 1063–1073.
- [54] J.N. Reddy, *An Introduction to the Finite Element Method*, McGraw-Hill, New York, 1993.